# Quantitative ImmunoPET of Prostate Cancer Xenografts with $^{89}$Zr- and $^{124}$I-Labeled Anti-PSCA A11 Minibody

Scott M. Knowles[1], Kirstin A. Zettlitz[1], Richard Tavaré[1], Matthew M. Rochefort[2], Felix B. Salazar[1], David B. Stout[1], Paul J. Yazaki[3], Robert E. Reiter[4], and Anna M. Wu[1]

*[1]Crump Institute for Molecular Imaging, Department of Molecular and Medical Pharmacology, David Geffen School of Medicine at the University of California–Los Angeles, Los Angeles, California; [2]Department of Surgery, David Geffen School of Medicine at the University of California–Los Angeles, Los Angeles, California; [3]Department of Immunology, Beckman Research Institute of the City of Hope, Duarte, California; and [4]Department of Urology, David Geffen School of Medicine at the University of California–Los Angeles, Los Angeles, California*

Prostate stem cell antigen (PSCA) is expressed on the cell surface in 83%–100% of local prostate cancers and 87%–100% of prostate cancer bone metastases. In this study, we sought to develop immunoPET agents using $^{124}$I- and $^{89}$Zr-labeled anti-PSCA A11 minibodies (scFv-$C_H$3 dimer, 80 kDa) and evaluate their use for quantitative immunoPET imaging of prostate cancer. **Methods:** A11 anti-PSCA minibody was alternatively labeled with $^{124}$I- or $^{89}$Zr-desferrioxamine and injected into mice bearing either matched 22Rv1 and 22Rv1× PSCA or LAPC-9 xenografts. Small-animal PET data were obtained and quantitated with and without recovery coefficient–based partial-volume correction, and the results were compared with ex vivo biodistribution. **Results:** Rapid and specific localization to PSCA-positive tumors and high-contrast imaging were observed with both $^{124}$I- and $^{89}$Zr-labeled A11 anti-PSCA minibody. However, the differences in tumor uptake and background uptake of the radiotracers resulted in different levels of imaging contrast. The nonresidualizing $^{124}$I-labeled minibody had lower tumor uptake (3.62 ± 1.18 percentage injected dose per gram [%ID/g] 22Rv1×PSCA, 3.63 ± 0.59 %ID/g LAPC-9) than the residualizing $^{89}$Zr-labeled minibody (7.87 ± 0.52 %ID/g 22Rv1×PSCA, 9.33 ± 0.87 %ID/g LAPC-9, $P < 0.0001$ for each), but the $^{124}$I-labeled minibody achieved higher imaging contrast because of lower nonspecific uptake and better tumor–to–soft-tissue ratios (22Rv1×PSCA:22Rv1 positive-to-negative tumor, 13.31 ± 5.59 $^{124}$I-A11 and 4.87 ± 0.52 $^{89}$Zr-A11, $P = 0.02$). Partial-volume correction was found to greatly improve the correspondence between small-animal PET and ex vivo quantification of tumor uptake for immunoPET imaging with both radionuclides. **Conclusion:** Both $^{124}$I- and $^{89}$Zr-labeled A11 anti-PSCA minibody showed high-contrast imaging of PSCA expression in vivo. However, the $^{124}$I-labeled A11 minibody was found to be the superior imaging agent because of lower nonspecific uptake and higher tumor–to–soft-tissue contrast. Partial-volume correction was found to be essential for robust quantification of immunoPET imaging with both $^{124}$I- and $^{89}$Zr-labeled A11 minibody.

**Key Words:** immunoPET; $^{89}$Zr; $^{124}$I; prostate stem cell antigen (PSCA); prostate cancer; minibody; antibody fragments; partial volume correction

**J Nucl Med 2014; 55:452–459**
DOI: 10.2967/jnumed.113.120873

ImmunoPET imaging is a powerful technique that has shown promise in noninvasive imaging of cell surface biomarkers with high specificity using radiolabeled antibodies and antibody fragments (*1*). Prostate stem cell antigen (PSCA) is a cell surface protein that has limited low-level expression in normal prostate, bladder, and stomach. PSCA, however, is expressed in 83%–100% of prostate cancers, where its expression correlates with the Gleason score and a poor prognosis (*2–6*). It is also highly expressed in most prostate cancer bone metastases (87%–100%), in many metastases to other sites (67%–95%), and in local bladder and pancreatic carcinoma (*5–10*). Our laboratory has previously shown that an $^{124}$I-labeled 2B3 anti-PSCA minibody, an engineered approximately 80 kDa antibody fragment (scFv-$C_H$3 homodimer, Fig. 1A), can target and image PSCA-expressing xenografts with high contrast at earlier time points than the intact 2B3 anti-PSCA antibody because of the minibody's faster clearance (*11,12*). Subsequent affinity maturation of the 2B3 minibody created the A11 anti-PSCA minibody, which showed improved immunoPET performance, and methods were established for current good manufacturing practices (cGMP) production and purification of this minibody (*13,14*). In the current work, we compare $^{124}$I and $^{89}$Zr radiolabels for immunoPET imaging using the affinity-matured cGMP-grade A11 anti-PSCA minibody and investigate quantitative immunoPET imaging with these alternative radionuclides. To assess the suitability of both $^{124}$I- and $^{89}$Zr-labeled A11 minibody for eventual use as clinical imaging agents capable of detecting both local prostate cancer and bone and soft-tissue metastases, we evaluated both the absolute tumor uptake and the tumor-to-non-tumor contrast obtainable with each radiolabel in preclinical mouse models.

The slow clearance of most immunoPET radiotracers requires late imaging time points (≥20 h after injection) that are beyond the limits of the most frequently used PET radionuclide, $^{18}$F, because of its short physical half-life ($t_{1/2}$ = 1.8 h, Table 1). Though strides have been made in optimizing fast-clearing immunoPET tracers that allow for $^{18}$F labeling, the 2 most promising positron-emitting radionuclides for mid- to late-time-point immunoPET are $^{124}$I and $^{89}$Zr because of their long physical $t_{1/2}$ (4.2 and 3.3 d, respectively) (*15*). Both $^{124}$I and $^{89}$Zr have advantages and disadvantages for use as PET tracers and differ with regard to physical properties, conjugation and required chelators, clearance, and uptake (*16*).

Received May 30, 2013; revision accepted Nov. 1, 2013.
For correspondence or reprints contact: Anna M. Wu, 570 Westwood Plaza, P.O. Box 951770, Los Angeles, CA 90095-1770.
E-mail: awu@mednet.ucla.edu
Published online Feb. 6, 2014.

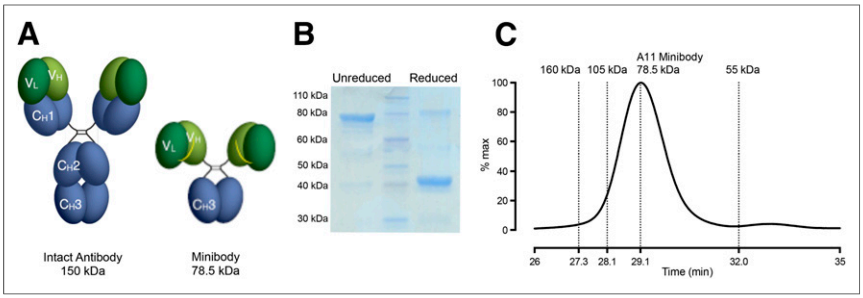


**FIGURE 1.** Cartoon representation of minibody, compared with intact antibody (A). SDS-PAGE (B) and size-exclusion chromatography (C) confirm that A11 minibody exists overwhelmingly as covalent scFv-$C_H3$ dimer with minimal amounts of monomer present.

$^{124}$I and $^{89}$Zr both suffer from low positron yields and emission of γ rays, which increase the absorbed dose to the patient. Quantitative PET imaging with $^{124}$I provides a challenge because of simultaneous emission of a 606-keV γ ray with 52% of positrons. This 606-keV γ ray falls into the energy window of most PET scanners and causes prompt γ coincidences, which increase the measured background in PET imaging by a factor ranging from 2.5 to 10 times that of $^{18}$F (*17*). $^{89}$Zr, on the other hand, emits a 909-keV γ ray with 100% of positrons but prompt γ coincidences do not occur both because the γ ray and positron emission are not simultaneous and because the γ ray is out of the scanner energy window (*18,19*).

PET imaging with $^{124}$I and $^{89}$Zr also suffers from lower effective resolution than $^{18}$F PET because the increased positron emission energy of $^{124}$I and $^{89}$Zr leads to a longer mean positron range (*16*). This increased positron range in turn contributes to a higher partial-volume effect (PVE) due to positrons traveling into voxels that neighbor where they were actually emitted. The PVE results in a lower measured activity in a hot region of interest (ROI) surrounded by a cold background than the true value due to positrons spilling out of the ROI, especially for small volumes (*20*). The reverse is also true: a cold ROI surrounded by a high-activity background will have a higher measured value than the true value due to activity spilling into the ROI. The PVE is not strictly a function of positron range: scanner resolution and the fact that an anatomic region may only partially occupy an image voxel also play a large role. However, the long positron range of $^{124}$I has been found to significantly increase the PVE in clinical PET scanners even in volumes 35 mm in diameter (*21*). The increased PVE due to positron range will especially affect small-animal PET scanning for which the scanner resolution (1.1–3.0 mm) is finer than the mean positron range of $^{124}$I and approaches the mean positron range of $^{89}$Zr, and the largest contributor to the PVE is the positron range (*18,22,23*).

In addition to their differences in the physical properties, $^{124}$I and $^{89}$Zr differ with regard to protein chemistry and biologic metabolism and can yield distinctly different results when used for immunoPET radiolabeling. $^{124}$I is generally randomly conjugated under oxidizing conditions to tyrosines present in the antibody. Once an $^{124}$I-labeled antibody is internalized and degraded, the $^{124}$I-iodide or $^{124}$I-iodotyrosine released is free to diffuse from the tissue, resulting in a loss of signal over time in target tissue but also low signal in background tissues and tissues of clearance (*24*). $^{89}$Zr, on the other hand, is most commonly conjugated onto antibodies in a 2-step process using the chelator desferrioxamine (DFO), which has previously been conjugated onto primary amines (N terminus and lysines) or free thiols (reduced cysteines) of the antibody (*19,25*). On internalization and catabolism, $^{89}$Zr-labeled radiometabolites are trapped in cellular lysosomes, allowing for higher retention of signal over time in target tissue than with $^{124}$I (*19*). Residualizing radiolabels such as $^{89}$Zr, however, often see higher uptake in organs of normal clearance (liver and kidney) and higher background uptake in other tissues that passively take up the antibody.

In the current study, we established a quantitative method of immunoPET imaging with $^{124}$I- and $^{89}$Zr-labeled A11 minibody that includes partial-volume correction to account for the long positron ranges of these isotopes. We then used quantitative immunoPET imaging to explore differences in tumor uptake and rates of tissue clearance with each of these radiotracers.

## MATERIALS AND METHODS

Details of protein production and purification, cell lines and xenografts, quantitative flow cytometry, cell binding and affinity studies, radiolabeling with $^{89}$Zr and $^{124}$I, in vitro cellular uptake studies, and biodistributions can be found in the supplemental materials (available at http://jnm.snmjournals.org).

### Small-Animal PET/CT

Approximately 25 μg (~4 MBq) of $^{124}$I-A11 or $^{89}$Zr-A11 with a purity of 98% or more were administered to tumor-bearing mice via tail vein injection. Before $^{124}$I-A11 administration, thyroid and stomach uptake of radioiodine was blocked, respectively, with Lugol iodine and potassium perchlorate as previously described (*13*). At 6, 20, and 44 h after injection, mice were anesthetized with 1.5% isoflurane anesthesia and imaged with 10-min acquisitions on an Inveon small-animal PET scanner (Siemens Preclinical Solutions), followed by a micro-CT scan (microCAT II; Siemens Preclinical Solutions) (*26*).

**TABLE 1**
Positron-Emitting Radionuclides for ImmunoPET

| Radionuclide | $t_{1/2}$ (h) | $\beta^+$ maximum energy (MeV) | $\beta^+$ mean range (mm) | $\beta^+$ maximum range (mm) | Positron yield (%) | Other gammas* (abundance) (keV) | Residualizing† |
|---|---|---|---|---|---|---|---|
| $^{18}$F | 1.8 | 0.6 | 0.5 | 2.3 | 97% | No | Yes |
| $^{89}$Zr | 78.4 | 0.9 | 1.1 | 3.6 | 23% | 909 (100%) | Yes |
| $^{124}$I | 100.2 | 2.1 | 3.0 | 10.2 | 24% | 603 (60%) | No |

*$^{124}$I also emits 723 keV (10%), 1,691 keV (10%), and other γ rays (6%) with lower abundance.
†Assumes antibody radiolabeling with $^{18}$F-SFB, $^{89}$Zr-DFO, and direct $^{124}$I iodination.

One mouse from each group also received a 2-h dynamic small-animal PET scan at the time of injection and additional scans at 4, 8, and 12 h after injection. Small-animal PET images were reconstructed by non–attenuation-corrected or scatter-corrected filtered backprojection and were analyzed and displayed using AMIDE (*27*). Coregistration of the small-animal PET and micro-CT scans was performed automatically using empirically determined scanner alignments.

### Image Quantitation and Partial-Volume Correction

Small-animal PET cylinder factors were measured by scanning a 2.5-cm-diameter cylinder containing various concentrations of $^{124}$I or $^{89}$Zr measured by dose calibrator (Atom Lab 300; Biodex Medical Systems). The mean PET value of each scan was obtained from a 1.5-cm-diameter ROI drawn at the center of the cylinder to avoid PVEs, and the cylinder factor was calculated by linear regression of the dose calibrator and PET values. The generation of recovery coefficient (RC) curves for partial-volume correction was performed by imaging spheres of varying size filled with identical concentrations of either $^{124}$I or $^{89}$Zr. Spheres of 8.0-mL, 4.0-mL, 2.0-mL, 1.0-mL, 0.5-mL, 250-μL, 125-μL, 63-μL, and 31-μL volumes (Data Spectrum Corp.) were measured. In addition, 20-μL, 10-μL, and 5-μL volumes were measured in 0.5-mL microcentrifuge tubes because appropriately sized hollow spheres are not commercially available. The mean $^{124}$I or $^{89}$Zr concentration obtained for each diameter ROI was converted into an RC by dividing the mean value measured by small-animal PET by the known value. The resulting curve was fit to a 2-parameter sigmoid function (Eq. 1), modified from Jentzen et al., where $a$ and $b$ are fitting parameters and $d$ is the diameter of the ROI in mm (*21*).

$$RC = \frac{1}{1 + (a/d)^b} \qquad \text{Eq. 1}$$

Tumor uptake values (%ID/$g_{ROI}$) and volumes were quantified by drawing elliptic ROIs over the entire tumor using the micro-CT. The ROI was subtlety repositioned (without changing the ROI dimensions), if required, to ensure placement over the tumor in the small-animal PET image because of small errors in small-animal PET/CT coregistration. The mean PET activity of the ROIs was converted to percentage injected dose per gram (%ID/g) using the decay-corrected injected dose and the cylinder factors for $^{89}$Zr and $^{124}$I, respectively, under the assumption that the density of the tumors was 1 g/mL. The RC of the ellipsoidal ROI was estimated by spheric approximation of the tumor volume ($d = \sqrt[3]{\frac{6V}{\pi}}$). The partial-volume–corrected %ID/g (%ID/$g_{PVC}$) was then calculated using Equation 2, where %ID/$g_{bkg}$ is the background activity obtained from the mean of ROIs drawn in the nonspecific tissue around the tumor (*28,29*). The subtraction of %ID/$g_{bkg}$ before dividing by the RC allows for simultaneous correction for spill-in and spill-out effects with no partial-volume correction in the case in which the ROI is drawn in a uniform background (*28*). The partial-volume correction method was validated by comparison of small-animal PET values to ex vivo biodistribution data in mice sacrificed immediately after imaging. Percentage error for this comparison was calculated as (%ID/$g_{ROI}$ − %ID/$g_{Biodist}$)/%ID/$g_{Biodist}$.

$$\%ID/g_{PVC} = \frac{\%ID/g_{ROI} - \%ID/g_{bkg}}{RC} + \%ID/g_{bkg} \qquad \text{Eq. 2}$$

### Data Analysis

Except where indicated otherwise, all values are reported as mean ± SD. Statistical analysis was performed using a 2-tailed Student $t$ test at the 95% confidence level ($P < 0.05$). The $P$ values obtained were adjusted for multiple comparisons via the Holm–Šidák method. Linear and nonlinear least-squares curve fitting was performed using GraphPad Prism 6.0. The linear fits of %ID/$g_{ROI}$ versus %ID/$g_{Biodist}$ were weighted by $1/y^2$ because the uncertainty of the small-animal PET value is proportional to the uptake. All small-animal PET/CT images are displayed as full-thickness maximum-intensity projections.

## RESULTS

### Antibody and Cell Line Characterization

SDS-PAGE and size exclusion confirm the A11 minibody is assembled as a covalent scFv-$C_H3$ 80 kDa homodimer comprising 40 kDa subunits (Fig. 1; Supplemental Fig. 1). Quantitative flow cytometry with the murine 1G8 anti-PSCA antibody ($n$ = 3) shows little or no expression of PSCA on 22Rv1 cells, expression of $2.2 \times 10^6$ PSCA antigens on 22Rv1×PSCA cells, and expression of $4.5 \times 10^5$ PSCA antigens on LAPC-9 cells (Fig. 2A). Flow cytometry shows specific binding of the A11 minibody to 22Rv1×PSCA cells with an apparent affinity of 13.7 ± 1.4 nM SEM (Fig. 2B). Measurement of A11 minibody binding on immobilized PSCA-mFc antigen using a quartz crystal microbalance shows an apparent affinity ($K_D$) of 3.91 nM. No loss of affinity is seen with iodinated A11 minibody ($K_D$ = 3.43 nM) and only a small decrease in affinity is seen with DFO-conjugated A11 minibody ($K_D$ = 6.75 nM), allowing for a direct comparison of $^{124}$I and $^{89}$Zr radiolabels with minimal effects from differences in minibody affinity (Supplemental Fig. 2).

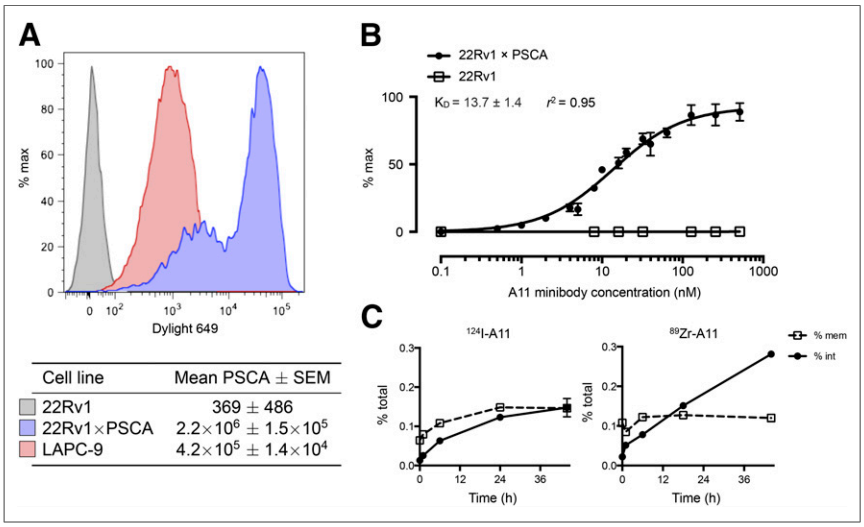


**FIGURE 2.** (A) Quantitative flow cytometry shows no expression of PSCA on 22Rv1 cells, high expression on 22Rv1×PSCA cells, and intermediate expression on disassociated LAPC-9 tumor cells ($n$ = 3 each). (B) Binding of A11 minibody to 22Rv1×PSCA cells has $K_D$ of 13.7 ± 1.4 nM as measured by flow cytometry. (C) Incubation of 22Rv1×PSCA cells with $^{124}$I-A11 and $^{89}$Zr-A11 demonstrates that PSCA slowly internalizes and that on internalization $^{89}$Zr residualizes and accumulates in cells to higher degree than $^{124}$I. Error bars are shown as ± SEM.

### Antibody Cell Binding and Uptake

In vitro antibody uptake experiments demonstrate antigen-specific binding and

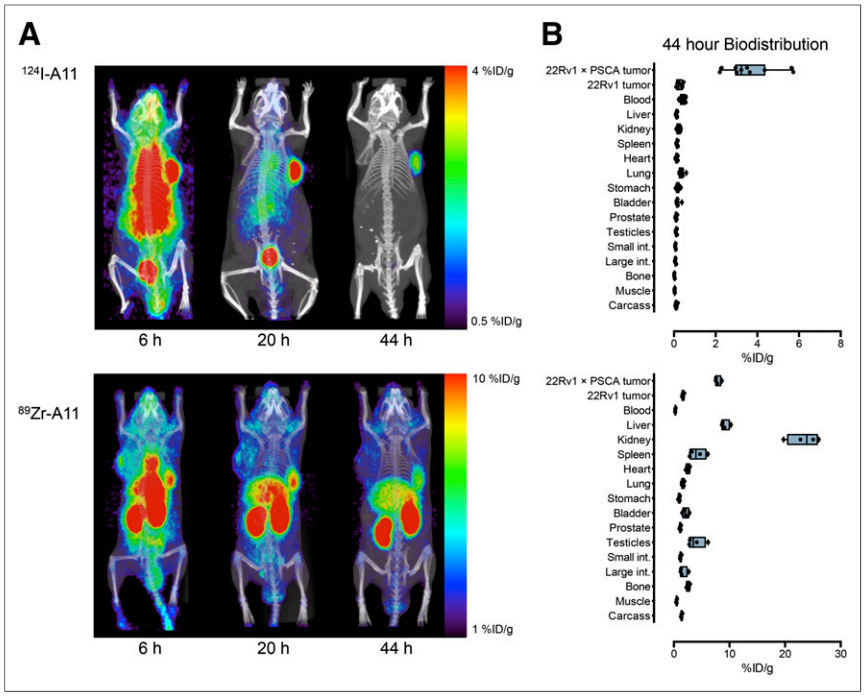


**FIGURE 3.** $^{124}$I-A11 vs. $^{89}$Zr-A11 immunoPET in mice bearing 22Rv1 (left) and 22Rv1×PSCA (right) subcutaneous tumors. Small-animal PET images (A) and ex vivo biodistribution (B) show higher positive tumor contrast when imaging with $^{124}$I-A11 than with $^{89}$Zr-A11, despite lower absolute uptake.

internalization of both $^{124}$I-A11 and $^{89}$Zr-A11 on 22Rv1×PSCA cells. However, $^{89}$Zr-A11 radiometabolites accumulate intracellularly to a higher degree than $^{124}$I-A11 radiometabolites over 44 h (Fig. 2C). These results are consistent with slow internalization of the PSCA, residualization of the $^{89}$Zr-A11 radiometabolites, and nonresidualization of the $^{124}$I-A11 radiometabolites as expected (*30*). 22Rv1 cells show no membrane binding or internalization of $^{89}$Zr-A11 or $^{124}$I-A11 at any time point (data not shown).

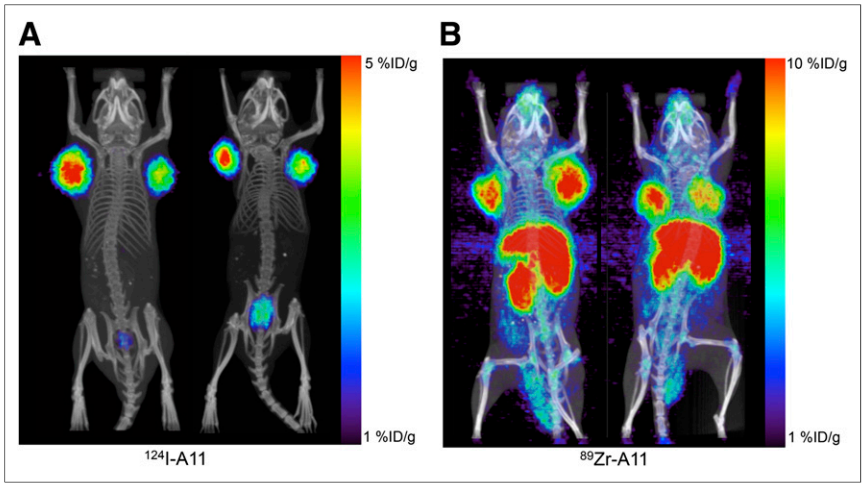


**FIGURE 4.** $^{124}$I-A11 vs. $^{89}$Zr-A11 immunoPET in SCID mice bearing bilateral LAPC-9 subcutaneous tumors at 44 h after injection shows higher contrast in tumors imaged with $^{124}$I-A11 despite higher absolute uptake in tumors imaged with $^{89}$Zr-A11. Small-animal PET images are shown as full-thickness maximum-intensity projections.

### Radiolabeling

$^{124}$I-A11 and $^{89}$Zr-A11 had mean specific activities of 141 ± 37 MBq/mg (3.8 ± 1.0 μCi/μg, $n$ = 7) and 115 ± 37 MBq/mg (3.1 ± 1.0 μCi/μg, $n$ = 3), respectively, with a radiochemical purity of 98% or more. Immunoreactivity of $^{124}$I-A11 and $^{89}$Zr-A11 were found to be 76.1% ± 9.7% ($n$ = 7) and 52.0% ± 9.2% ($n$ = 3), respectively, as measured by cellular association with excess 22Rv1×PSCA cells, with 5% or less binding to the negative control 22Rv1 cell line. Stability of $^{89}$Zr-A11 and $^{124}$I-A11 in both 1% fetal bovine serum/phosphate-buffered saline and mouse serum was 95% or more at 44 h.

### In Vivo Characterization of $^{124}$I-A11 and $^{89}$Zr-A11 Minibody

Both $^{124}$I-A11 and $^{89}$Zr-A11 demonstrate specific uptake in antigen-positive 22Rv1×PSCA tumors, with uptake significantly higher than in 22Rv1 control tumors ($P <$ 0.0001 for each, Fig. 3). LAPC-9 tumors showed similarly high levels of uptake, and high-contrast imaging was obtained with both radiotracers (Fig. 4). $^{89}$Zr-A11 demonstrates significantly higher tumor uptake and higher tumor-to-blood ratios than $^{124}$I-A11 in both 22Rv1×PSCA (Table 2) and LAPC-9 xenografts (Table 3) at 44 h after injection. However, $^{89}$Zr-A11 also demonstrates nonspecific background uptake, especially in the liver, kidneys, and spleen, but also in all other tissues measured, which all show activity higher than blood at 44 h after injection. Mice injected with $^{124}$I-A11, on the other hand, show uptake lower than blood in all organs other than the 22Rv1×PSCA and LAPC-9 tumors. $^{124}$I-A11 shows a 22Rv1×PSCA:22Rv1 tumor ratio of 13.3 and tumor-to-muscle ratio of 133.3 whereas with $^{89}$Zr-89 the 22Rv1×PSCA:22Rv1 tumor ratio was 4.9 and the tumor-to-muscle ratio was 15.9. In fact, other than the tumor-to-blood ratio, every tumor-to-nontumor ratio was higher for $^{124}$I-A11 than for $^{89}$Zr-A11 in both 22Rv1×PSCA–bearing nude mice and LAPC-9–bearing severe-combined immunodeficiency (SCID) mice, allowing for much better image contrast with $^{124}$I-A11 than with $^{89}$Zr-A11 (Figs. 3 and 4).

### Quantification of $^{124}$I-A11 and $^{89}$Zr-A11 Small-Animal PET and Comparison to Biodistribution

RC curves generated for $^{124}$I and $^{89}$Zr demonstrate that the higher positron emission energy and longer mean positron range of $^{124}$I has a detrimental effect on effective scanner resolution and increases the PVE, compared with $^{89}$Zr (Fig. 5). Comparison of non–partial-volume–corrected small-animal PET ROI analysis and biodistribution reveals

**TABLE 2**
44-Hour Biodistribution of Male Nude Mice Bearing 22Rv1 (Negative) and 22Rv1×PSCA (Positive) Xenografts

| Organ | $^{124}$I-A11 | | $^{89}$Zr-A11 | | |
|---|---|---|---|---|---|
| | *n* | %ID/g ± SD | *n* | %ID/g ± SD | *P* |
| 22Rv1×PSCA | 11 | 3.62 ± 1.18 | 4 | 7.87 ± 0.52 | <0.0001 |
| 22Rv1 | 8 | 0.34 ± 0.26 | 4 | 1.63 ± 0.18 | <0.0001 |
| Blood | 13 | 0.41 ± 0.11 | 4 | 0.26 ± 0.05 | 0.03 |
| Liver | 13 | 0.12 ± 0.02 | 4 | 9.19 ± 0.74 | <0.0001 |
| Kidney | 13 | 0.21 ± 0.08 | 4 | 23.39 ± 2.82 | <0.0001 |
| Spleen | 10 | 0.14 ± 0.04 | 4 | 4.22 ± 1.50 | <0.0001 |
| Heart | 13 | 0.12 ± 0.04 | 4 | 2.54 ± 0.33 | <0.0001 |
| Lung | 11 | 0.37 ± 0.12 | 4 | 1.64 ± 0.24 | <0.0001 |
| Stomach | 10 | 0.19 ± 0.07 | 4 | 0.99 ± 0.17 | <0.0001 |
| Bladder | 8 | 0.17 ± 0.09 | 4 | 2.11 ± 0.55 | <0.0001 |
| Prostate | 8 | 0.11 ± 0.03 | 4 | 1.17 ± 0.14 | <0.0001 |
| Testicles | 5 | 0.11 ± 0.03 | 4 | 3.98 ± 1.57 | 0.001 |
| Small intestine | 5 | 0.07 ± 0.02 | 4 | 1.20 ± 0.13 | <0.0001 |
| Large intestine | 5 | 0.07 ± 0.03 | 4 | 1.64 ± 0.70 | 0.001 |
| Bone | 5 | 0.02 ± 0.01 | 4 | 2.54 ± 0.28 | <0.0001 |
| Muscle | 12 | 0.03 ± 0.01 | 4 | 0.50 ± 0.08 | <0.0001 |
| Carcass | 13 | 0.10 ± 0.03 | 4 | 1.39 ± 0.11 | <0.0001 |
| Ratio (unitless) | | | | | |
| Positive-to-negative tumor | 5 | 13.31 ± 5.59 | 4 | 4.87 ± 0.52 | 0.02 |
| Tumor to blood | 11 | 8.65 ± 2.62 | 4 | 30.36 ± 5.05 | <0.0001 |
| Tumor to muscle | 10 | 133.33 ± 51.9 | 4 | 15.86 ± 2.10 | 0.0008 |

a large underestimate of tumor uptake for both $^{124}$I and $^{89}$Zr, especially for small tumors (−43.7% ± 15.7% and −24.09% ± 19.49% mean percentage error, respectively; Figs. 5E and 5F in blue). RC-based partial-volume correction both improves correspondence with ex vivo biodistribution and reduces the variance for both $^{124}$I and $^{89}$Zr uptake, resulting in respective mean percentage errors of −0.4% ± 13.5% and 5.19% ± 8.45% after partial-volume correction (Figs. 5E and 5F in red).

Dynamic imaging of both $^{124}$I-A11 and $^{89}$Zr-A11 shows peak uptake in 22Rv1×PSCA tumors at 12 h after injection. Tumor uptake then falls 49% from its peak over the next 32 h for the $^{124}$I-labeled minibody where catabolized radiometabolites do not residualize and can diffuse from the tumor. $^{89}$Zr-labeled radiometabolites, on the other hand, residualize and diffuse more slowly out of the tumor, and hence 22Rv1×PSCA tumor uptake decreases by only 19% between 12 and 44 h (Figs. 6A and 6B). Averages from serial imaging of 22Rv1×PSCA–bearing mice with $^{89}$Zr-A11 and $^{124}$I-A11 at 6, 20, and 44 h after injection similarly show significantly higher uptake and higher retention of $^{89}$Zr-A11 ($n = 4$) than $^{124}$I-A11 ($n = 6$) at all time points (Fig. 6D). Quantitation of dynamic imaging also demonstrates that while a left ventricular ROI can be used for estimating the activity in the blood pool with $^{124}$I-A11 by small-animal PET, the quantification of the blood activity with $^{89}$Zr-A11 using this method is confounded by nonspecific uptake in the heart wall in excess of that present in the blood. The spill-in from the heart wall results in an overestimation of blood activity of $^{89}$Zr-A11 at late time points and negates the ability to accurately quantify blood activity and tumor-to-blood ratios from a heart ROI (Figs. 6B and 6C). At 44 h after injection, comparison of blood activities by small-animal PET heart ROIs

**TABLE 3**
44-Hour Biodistribution of Male SCID Mice Bearing Bilateral LAPC-9 Xenografts

| Organ | $^{124}$I-A11 | | $^{89}$Zr-A11 | | |
|---|---|---|---|---|---|
| | *n* | %ID/g ± SD | *n* | %ID/g ± SD | *P* |
| LAPC-9 | 9 | 3.63 ± 0.59 | 6 | 9.33 ± 0.87 | <0.0001 |
| Blood | 5 | 0.65 ± 0.11 | 3 | 0.74 ± 0.17 | 0.41 |
| Liver | 5 | 0.19 ± 0.01 | 3 | 14.61 ± 0.11 | <0.0001 |
| Kidney | 5 | 0.26 ± 0.03 | 3 | 16.10 ± 2.74 | <0.0001 |
| Spleen | 5 | 0.27 ± 0.04 | 3 | 24.81 ± 6.64 | <0.0001 |
| Heart | 5 | 0.32 ± 0.06 | 3 | 4.14 ± 0.45 | 0.0001 |
| Stomach | 5 | 0.38 ± 0.09 | 3 | 1.74 ± 0.26 | <0.0001 |
| Lung | 5 | 0.54 ± 0.08 | 3 | 2.74 ± 1.02 | 0.002 |
| Muscle | 5 | 0.05 ± 0.02 | 3 | 0.67 ± 0.11 | <0.0001 |
| Carcass | 5 | 0.13 ± 0.02 | 3 | 1.82 ± 0.12 | 0.0001 |
| Ratio (unitless) | | | | | |
| Tumor to blood | 9 | 5.58 ± 1.07 | 6 | 13.16 ± 3.34 | <0.0001 |
| Tumor to muscle | 9 | 74.01 ± 29.1 | 6 | 14.03 ± 1.84 | 0.0003 |

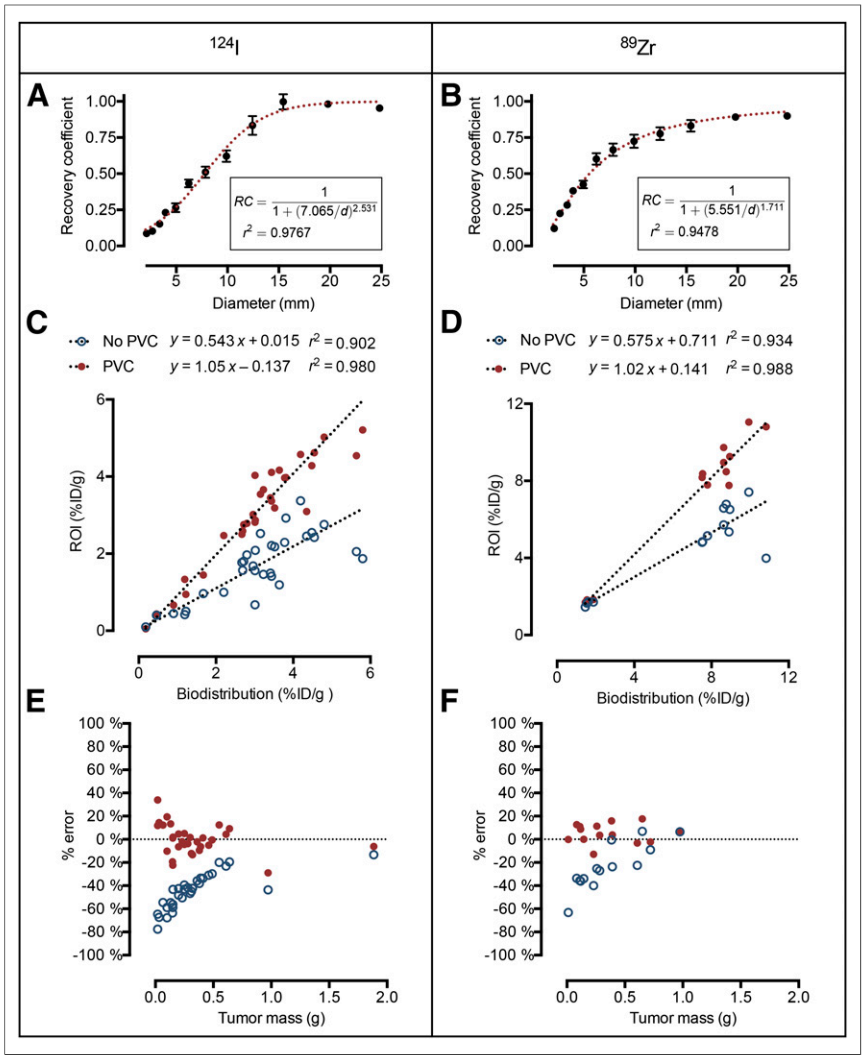


**FIGURE 5.** RC curves for $^{124}$I and $^{89}$Zr show higher PVE for $^{124}$I (A) than for $^{89}$Zr (B). Quantitation of tumor uptake from small-animal PET images shows that non-PVC–corrected ROIs underestimate uptake of $^{124}$I-A11 (C and E) and $^{89}$Zr-A11 (D and F), especially for tumors of small size. Partial-volume–corrected small-animal PET data show better correspondence with biodistribution for both $^{124}$I-A11 and $^{89}$Zr-A11.

and ex vivo biodistribution shows excellent correspondence for $^{124}$I-A11 (0.56 ± 0.13 %ID/$g_{Biodist}$ vs. 0.59 ± 0.19 %ID/$g_{PVC}$, $n = 20$, $P = 0.593$) but poor correspondence for $^{89}$Zr-A11, with the heart ROI significantly overestimating the activity in the blood pool (0.47 ± 0.27 %ID/$g_{Biodist}$ vs. 2.02 ± 0.47 %ID/$g_{PVC}$, $n = 7$, $P < 10^{-5}$). As a result, small-animal PET quantification of tumor-to-blood ratios using tumor and heart ROIs is accurate for $^{124}$I-A11 (mean tumor-to-blood ratio, 6.00 ± 2.39 biodistribution vs. 5.93 ± 2.75 small-animal PET, $n = 28$, $P = 0.92$) but greatly underestimates the tumor-to-blood ratio for $^{89}$Zr-A11 (mean tumor-to-blood ratio, 20.04 ± 9.67 biodistribution vs. 4.41 ± 0.93, $n = 10$, $P < 0.0001$).

## DISCUSSION

In this work, we evaluated two alternative means of radiolabeling the A11 anti-PSCA minibody for imaging two PSCA-expressing tumors. $^{124}$I-A11 and $^{89}$Zr-A11 both show uptake in PSCA-expressing 22Rv1×PSCA and LAPC-9 tumors and result in high-contrast small-animal PET imaging. The rapid clearance of the minibody is advantageous for imaging with $^{124}$I-A11, for which excellent tumor contrast is seen, with uptake nearly an order of magnitude higher in the tumor than in any other organ at 44 h after injection. The residualizing nature of $^{89}$Zr-A11 results in 2- to 3-fold higher uptake and retention of tumor activity in both 22Rv1×PSCA and LAPC-9 tumor models, resulting in 2- to 3-fold higher tumor-to-blood ratios at 44 h than obtained with $^{124}$I-A11. $^{89}$Zr-A11, however, displays significantly increased background, compared with $^{124}$I-A11, in all nontumor tissue of both nude and SCID mice and results in lower tumor–to–soft-tissue contrast for $^{89}$Zr-A11 by both small-animal PET imaging and biodistribution. The nonspecific uptake in the bone and liver for $^{89}$Zr-A11 is especially problematic because these are common sites of prostate cancer metastases and may interfere with the detection of tumors in these locations.

Quickly clearing antibody fragments such as minibodies generally have lower uptake in tumors than intact antibodies because of shorter time allowed for extravasation from the vasculature and diffusion into the tissue. However, the minibody's short residence time in the blood compensates for the lower absolute tumor uptake, allowing higher tumor-to-blood ratios and improved imaging contrast at early time points (*12,31*). The short $t_{1/2}$ of the A11 minibody ($t_{1/2\beta} \approx 6$ h) also has the benefit of reducing the radioactivity exposure and absorbed dose to the patient.$^{124}$I-A11 minibody and its radiometabolites clear the body quickly, and $^{124}$I-labeled probes are usually dose-limited only by bone marrow dose via cross-exposure from the blood, which will decrease when using quickly clearing $^{124}$I-labeled minibodies (*32*). The increased background uptake of $^{89}$Zr-A11 and its radiometabolites, on the other hand, will result in smaller improvements in patient dosimetry for the minibody than for an intact antibody. Dosimetry studies of other $^{89}$Zr-DFO–labeled antibodies have suggested that nonspecific accumulation of the radiometabolite in the liver or kidney will be dose-limiting, which will also likely be the case for $^{89}$Zr-A11 minibody (*33–35*).

Quantification of PET data from $^{89}$Zr and $^{124}$I is more challenging than with $^{18}$F, because of their lower positron yield and higher position emission energy, which leads to a long mean positron range, especially for $^{124}$I. Though the 603-keV γ ray of $^{124}$I falls into the energy window of the Inveon scanner and elevates measurements of relatively cold image areas, small-animal PET shows a remarkably linear response to varying concentrations of both $^{124}$I and $^{89}$Zr (Supplemental Fig. 3) (*17*). The increased positron range of $^{89}$Zr, and especially $^{124}$I, however, leads to a large PVE that cannot be ignored when quantifying small-animal PET imaging data with these isotopes. Measurements of in vivo tumor uptake

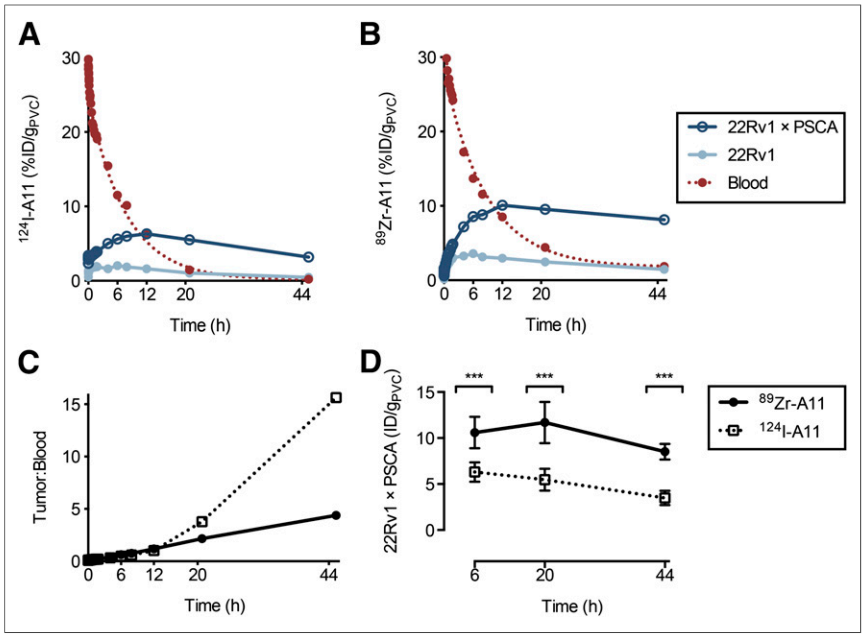


**FIGURE 6.** Quantification of dynamic and serial imaging with $^{124}$I-A11 (A) and $^{89}$Zr-A11 (B) demonstrates higher uptake and retention of A11 minibody with $^{89}$Zr labeling than with $^{124}$I labeling. Blood uptake as quantified by heart ROI shows artificially elevated signal for $^{89}$Zr-A11 at late time points due to nonspecific uptake in the heart wall leading to underestimations of tumor-to-blood ratio when quantified with heart ROIs. (C) However, $^{124}$I-A11 blood activity and tumor-to-blood ratios can be accurately quantified by this method. (D) Serial imaging of $^{89}$Zr-A11 ($n = 4$) and $^{124}$I-A11 ($n = 6$) mice bearing 22Rv1×PSCA xenografts confirms results of dynamic scans. ***$P < 0.0001$.

without partial-volume correction underestimate the amount of uptake, especially for small tumors, and significant differences in uptake between tumor groups could easily be observed simply because of differences in the mean size of the tumors imaged. Correcting for the PVE is especially important when imaging response to therapy, in which what appears to be a downregulation of immunoPET uptake with treatment could simply be an artifact of a smaller average tumor in the treated group.

The partial-volume correction method used here requires fairly precise approximation of tumor volumes both for accurate determination of the mean PET uptake and for determination of the tumor volume from which the RC is calculated. Though precise determination of tumor volume is time-consuming and some intraoperator variability can be expected with any manual ROI drawing procedure, determination of tumor volumes from CT has been found to be more accurate than determination of tumor volume through the use of PET data or caliper measurements, with excellent correspondence between observers ($r^2 = 0.97$) (*36*). The CT tumor volumes determined here correspond well with ex vivo tumor masses, with the CT volumes underestimating the tumor mass by only 8% on average (slope = 0.92, $r^2 = 0.96$, Supplemental Fig. 4). Most of the underestimations of the tumor volume are due to measurements of larger tumors, which tend to be more irregularly shaped and therefore more difficult to approximate with an ellipsoid ROI. However, precise determination of tumor volume for partial-volume correction is less important for large tumors, as the RC curve approaches 1 at large diameters. Despite the limitations of manual ROI drawing, the partial-volume–corrected estimation of tumor activity is considerably more accurate and less noisy than other common methods of quantification, including the commonly used estimation from the maximum voxel in the image, which both exhibits a strong PVE and is more noisy than using the mean value, making partial-volume correction harder to apply (13.9% ± 30.8% $^{124}$I mean percentage error and 10.87% ± 26.57% $^{89}$Zr mean percentage error, Supplemental Fig. 5).

In summary, residualizing radiolabels such as $^{89}$Zr are essential for imaging rapidly internalizing antigens where the radiolabel can be accumulated and concentrated intracellularly, using nonresidualizing antibodies on rapidly internalizing antigens will result in low tumor uptake due to internalization and loss of signal through diffusion. When imaging noninternalizing antigens, on the other hand, image contrast is improved using a nonresidualizing radiolabel such as $^{124}$I because of lower nonspecific accumulation. With slowly internalizing antigens, such as PSCA, the choice of a residualizing or nonresidualizing radiolabel is a compromise between higher tumor uptake for the residualizing label and lower background for the nonresidualizing label that will vary with the choice of particular antigen and imaging agent $t_{1/2}$. For imaging of PSCA expression with the A11 minibody, this balance clearly lies with the nonresidualizing $^{124}$I radiolabel and as such we have recently entered clinical evaluation of $^{124}$I-A11.

Quantitative small-animal PET imaging with $^{124}$I and $^{89}$Zr must take into account the long mean positron range of these isotopes. Partial-volume correction even with a simple RC-based method and a spheric approximation of the tumors greatly improves the correspondence between small-animal PET and ex vivo quantification. Further improvement can likely be seen with more advanced partial-volume correction methods (*37*).

## CONCLUSION

This work showed rapid targeting and high-contrast imaging of PSCA-expressing prostate cancer xenografts using both $^{124}$I- and $^{89}$Zr-labeled A11 minibody. Although the $^{89}$Zr-labeled antibody achieved higher tumor uptake at 44 h after injection, the $^{124}$I-labeled antibody showed lower background and higher tumor–to–soft-tissue contrast. $^{124}$I was therefore determined to be the preferred radiolabel for A11 minibody immunoPET. Partial-volume correction greatly improved the correspondence of small-animal PET, and ex vivo biodistribution was found to be essential for quantification of small-animal PET data with both $^{89}$Zr and $^{124}$I radiolabels.

## DISCLOSURE

The costs of publication of this article were defrayed in part by the payment of page charges. Therefore, and solely to indicate fact, this article is hereby marked "advertisement" in accordance with 18 USC section 1734. This work was supported by grants CA092131 and CA016042 from the National Institutes of Health, W81WXH-08-1-0442 from the Department of Defense, DE-SC0001220 from the Department of Energy, NIH T32 GM008042 from the UCLA-Caltech

Medical Scientist Training Program, and F30CA165824 NRSA Fellowship Award from the National Cancer Institute. Robert E. Reiter and Anna M. Wu are shareholders and consultants of ImaginAb Inc., which has licensed some of the technology described in this manuscript. No other potential conflict of interest relevant to this article was reported.

## ACKNOWLEDGMENTS

We thank Waldemar Ladno, Darin Williams, Melissa McCracken, Dr. John David, and Dr. Magnus Dahlbom for technical assistance with these experiments.

## REFERENCES

1. Knowles SM, Wu AM. Advances in immuno-positron emission tomography: antibodies for molecular imaging in oncology. *J Clin Oncol.* 2012;30:3884–3892.
2. Reiter RE, Gu Z, Watabe T, et al. Prostate stem cell antigen: a cell surface marker overexpressed in prostate cancer. *Proc Natl Acad Sci USA.* 1998;95:1735–1740.
3. Han KR, Seligson DB, Liu X, et al. Prostate stem cell antigen expression is associated with Gleason score, seminal vesicle invasion and capsular invasion in prostate cancer. *J Urol.* 2004;171:1117–1121.
4. Barbisan F, Mazzucchelli R, Santinelli A, et al. Expression of prostate stem cell antigen in high-grade prostatic intraepithelial neoplasia and prostate cancer. *Histopathology.* 2010;57:572–579.
5. Gu Z, Thomas G, Yamashiro J, et al. Prostate stem cell antigen (PSCA) expression increases with high Gleason score, advanced stage and bone metastasis in prostate cancer. *Oncogene.* 2000;19:1288–1296.
6. Zhigang Z, Wenlv S. Prostate stem cell antigen (PSCA) expression in human prostate cancer tissues: implications for prostate carcinogenesis and progression of prostate cancer. *Jpn J Clin Oncol.* 2004;34:414–419.
7. Lam JS, Yamashiro J, Shintaku IP, et al. Prostate stem cell antigen is overexpressed in prostate cancer metastases. *Clin Cancer Res.* 2005;11:2591–2596.
8. Amara N, Palapattu GS, Schrage M, et al. Prostate stem cell antigen is overexpressed in human transitional cell carcinoma. *Cancer Res.* 2001;61:4660–4665.
9. Wente MN, Jain A, Kono E, et al. Prostate stem cell antigen is a putative target for immunotherapy in pancreatic cancer. *Pancreas.* 2005;31:119–125.
10. Ananias HJK, van den Heuvel MC, Helfrich W, de Jong IJ. Expression of the gastrin-releasing peptide receptor, the prostate stem cell antigen and the prostate-specific membrane antigen in lymph node and bone metastases of prostate cancer. *Prostate.* 2009;69:1101–1108.
11. Olafsen T, Gu Z, Sherman MA, et al. Targeting, imaging, and therapy using a humanized antiprostate stem cell antigen (PSCA) antibody. *J Immunother.* 2007;30:396–405.
12. Leyton JV, Olafsen T, Lepin EJ, et al. Humanized radioiodinated minibody for imaging of prostate stem cell antigen-expressing tumors. *Clin Cancer Res.* 2008;14:7488–7496.
13. Lepin EJ, Leyton JV, Zhou Y, et al. An affinity matured minibody for PET imaging of prostate stem cell antigen (PSCA)-expressing tumors. *Eur J Nucl Med Mol Imaging.* 2010;37:1529–1538.
14. Gagnon P, Cheung CW, Lepin EJ, et al. Minibodies and multimodal chromatography methods: a convergence of challenge and opportunity. *Bioprocess Int.* 2010;8:26–35.
15. Olafsen T, Sirk SJ, Olma S, Shen CKF, Wu AM. ImmunoPET using engineered antibody fragments: fluorine-18 labeled diabodies for same-day imaging. *Tumour Biol.* 2012;33:669–677.
16. Nayak TK, Brechbiel MW. Radioimmunoimaging with longer-lived positron-emitting radionuclides: potentials and challenges. *Bioconjug Chem.* 2009;20:825–841.
17. Herzog H, Tellman L, Qaim SM, Spellerberg S, Schmid A, Coenen HH. PET quantitation and imaging of the non-pure positron-emitting iodine isotope $^{124}$I. *Appl Radiat Isot.* 2002;56:673–679.
18. Lubberink M, Herzog H. Quantitative imaging of $^{124}$I and 86Y with PET. *Eur J Nucl Med Mol Imaging.* 2011;38(suppl 1):S10–S18.
19. Deri MA, Zeglis BM, Francesconi LC, Lewis JS. PET imaging with $^{89}$Zr: from radiochemistry to the clinic. *Nucl Med Biol.* 2013;40:3–14.
20. Soret M, Bacharach SL, Buvat I. Partial-volume effect in PET tumor imaging. *J Nucl Med.* 2007;48:932–945.
21. Jentzen W, Weise R, Kupferschläger J, et al. Iodine-124 PET dosimetry in differentiated thyroid cancer: recovery coefficient in 2D and 3D modes for PET(/CT) systems. *Eur J Nucl Med Mol Imaging.* 2008;35:611–623.
22. Visser EP, Disselhorst JA, Brom M, et al. Spatial resolution and sensitivity of the Inveon small-animal PET scanner. *J Nucl Med.* 2009;50:139–147.
23. Sanchez-Crespo A. Comparison of gallium-68 and fluorine-18 imaging characteristics in positron emission tomography. *Appl Radiat Isot.* 2013;76:55–62.
24. van Dongen GA, Visser GW, Lub-de Hooge MN, de Vries EG, Perk LR.Immuno-PET: a navigator in monoclonal antibody development and applications. *Oncologist.* 2007;12:1379–1389.
25. Tinianow JN, Gill HS, Ogasawara A, et al. Site-specifically $^{89}$Zr-labeled monoclonal antibodies for immunoPET. *Nucl Med Biol.* 2010;37:289–297.
26. Bao Q, Newport D, Chen M, Stout DB, Chatziioannou AF. Performance evaluation of the Inveon dedicated PET preclinical tomograph based on the NEMA NU-4 standards. *J Nucl Med.* 2009;50:401–408.
27. Loening AM, Gambhir SS. AMIDE: a free software tool for multimodality medical image analysis. *Mol Imaging.* 2003;2:131–137.
28. Rousset GO, Zaidiy H. Correction for partial volume effects in emission tomography. In: Zaidi H, ed. *Quantitative Analysis of Nuclear Medicine Images.* New York, NY: Springer Science+Business Media; 2006:236–271.
29. Kessler RM, Ellis JR, Eden M. Analysis of emission tomographic scan data: limitations imposed by resolution and background. *J Comput Assist Tomogr.* 1984;8:514–522.
30. Ross S, Spencer SD, Holcomb I, et al. Prostate stem cell antigen as therapy target: tissue expression and in vivo efficacy of an immunoconjugate. *Cancer Res.* 2002;62:2546–2553.
31. Wu AM, Senter PD. Arming antibodies: prospects and challenges for immunoconjugates. *Nat Biotechnol.* 2005;23:1137–1146.
32. Schwartz J, Humm JL, Divgi CR, Larson SM, O'Donoghue JA. Bone marrow dosimetry using $^{124}$I-PET. *J Nucl Med.* 2012;53:615–621.
33. Börjesson PK, Jauw YW, Boellaard R, et al. Performance of immuno-positron emission tomography with zirconium-89-labeled chimeric monoclonal antibody U36 in the detection of lymph node metastases in head and neck cancer patients. *Clin Cancer Res.* 2006;12:2133–2140.
34. Börjesson PKE, Jauw YWS, de Bree R, et al. Radiation dosimetry of $^{89}$Zr-labeled chimeric monoclonal antibody U36 as used for immuno-PET in head and neck cancer patients. *J Nucl Med.* 2009;50:1828–1836.
35. Holland JP, Divilov V, Bander NH, Smith-Jones PM, Larson SM, Lewis JS. $^{89}$Zr-DFO-J591 for immunoPET of prostate-specific membrane antigen expression in vivo. *J Nucl Med.* 2010;51:1293–1300.
36. Jensen MM, Jørgensen JT, Binderup T, Kjaer A. Tumor volume in subcutaneous mouse xenografts measured by microCT is more accurate and reproducible than determined by $^{18}$F-FDG-microPET or external caliper. *BMC Med Imaging.* 2008;8:16.
37. Erlandsson K, Buvat I, Pretorius PH, Thomas BA, Hutton BF. A review of partial volume correction techniques for emission tomography and their applications in neurology, cardiology and oncology. *Phys Med Biol.* 2012;57:R119–R159.